nanomaterials

MDPI

Article

A-Site Cation Size Effect on Structure and Magnetic Properties of Sm(Eu,Gd)$Cr_{0.2}Mn_{0.2}Fe_{0.2}Co_{0.2}Ni_{0.2}O_3$ High-Entropy Solid Solutions

Denis A. Vinnik [1], Vladimir E. Zhivulin [1], Evgeny A. Trofimov [1], Svetlana A. Gudkova [1], Alexander Yu. Punda [1], Azalia N. Valiulina [1], Maksim Gavrilyak [1], Olga V. Zaitseva [1], Sergey V. Taskaev [1], Mayeen Uddin Khandaker [2], Amal Alqahtani [3], David A. Bradley [2,4], M. I. Sayyed [5,6], Vitaliy A. Turchenko [1,7,8], Alex V. Trukhanov [1,9,10] and Sergei V. Trukhanov [1,9,*]

1 Laboratory of Single Crystal Growth, South Ural State University, 76, Lenin Av., 454080 Chelyabinsk, Russia; denisvinnik@gmail.com (D.A.V.); zhivulinve@susu.ru (V.E.Z.); tea7510@gmail.com (E.A.T.); svetlanagudkova@yandex.ru (S.A.G.); pundaai@susu.ru (A.Y.P.); an_valiulina@mai.ru (A.N.V.); gavrilyak.maksim@yandex.ru (M.G.); nikonovaolga90@gmail.com (O.V.Z.); s.v.taskaev@gmail.com (S.V.T.); va_turchenko@mail.ru (V.A.T.); truhanov86@mail.ru (A.V.T.)
2 Centre for Applied Physics and Radiation Technologies, School of Engineering and Technology, Sunway University, Bandar Sunway 47500, Selangor, Malaysia; mayeenk@sunway.edu.my (M.U.K.); d.a.bradley@surrey.ac.uk (D.A.B.)
3 Department of Basic Sciences, Deanship of Preparatory Year and Supporting Studies, Imam Abdulrahman Bin Faisal University, P.O. Box 1982, Dammam 34212, Saudi Arabia; amalqahtani@iau.edu.sa
4 Centre for Nuclear and Radiation Physics, Department of Physics, University of Surrey, Guildford GU2 7XH, Surrey, UK
5 Department of Physics, Faculty of Science, Isra University, Amman 11622, Jordan; dr.mabualssayed@gmail.com
6 Department of Nuclear Medicine Research, Institute for Research and Medical Consultations (IRMC), Imam Abdulrahman Bin Faisal University, Dammam 31441, Saudi Arabia
7 Laboratory of Neutron Physics, Joint Institute for Nuclear Research, 6, Joliot-Curie Str., 141980 Dubna, Russia
8 Donetsk Institute of Physics and Technology Named after O.O. Galkin of the NASU, 46, Nauki Av., 03680 Kiev, Ukraine
9 Laboratory of Magnetic Films Physics, SSPA "Scientific and Practical Materials Research Centre of NAS of Belarus", 19, P. Brovki str., 220072 Minsk, Belarus
10 L.N. Gumilyov Eurasian National University, 2, Satpayev str., Nur-Sultan 010000, Kazakhstan
* Correspondence: sv_truhanov@mail.ru; Tel.: +375-29-536-86-19

check for updates

Citation: Vinnik, D.A.; Zhivulin, V.E.; Trofimov, E.A.; Gudkova, S.A.; Punda, A.Y.; Valiulina, A.N.; Gavrilyak, M.; Zaitseva, O.V.; Taskaev, S.V.; Khandaker, M.U.; et al. A-Site Cation Size Effect on Structure and Magnetic Properties of Sm(Eu,Gd)$Cr_{0.2}Mn_{0.2}Fe_{0.2}Co_{0.2}Ni_{0.2}O_3$ High-Entropy Solid Solutions. *Nanomaterials* **2022**, *12*, 36. https://doi.org/10.3390/nano12010036

Academic Editor: Alain Pignolet

Received: 3 December 2021
Accepted: 21 December 2021
Published: 23 December 2021

Publisher's Note: MDPI stays neutral with regard to jurisdictional claims in published maps and institutional affiliations.

Abstract: Three high-entropy Sm(Eu,Gd)$Cr_{0.2}Mn_{0.2}Fe_{0.2}Co_{0.2}Ni_{0.2}O_3$ perovskite solid solutions were synthesized using the usual ceramic technology. The XRD investigation at room temperature established a single-phase perovskite product. The Rietveld refinement with the FullProf computer program in the frame of the orthorhombic Pnma (No 62) space group was realized. Along with a decrease in the V unit cell volume from ~224.33 Å^3 for the Sm-based sample down to ~221.52 Å^3 for the Gd-based sample, an opposite tendency was observed for the unit cell parameters as the ordinal number of the rare-earth cation increased. The average grain size was in the range of 5–8 μm. Field magnetization was measured up to 30 kOe at 50 K and 300 K. The law of approach to saturation was used to determine the M_s spontaneous magnetization that nonlinearly increased from ~1.89 emu/g (Sm) up to ~17.49 emu/g (Gd) and from ~0.59 emu/g (Sm) up to ~3.16 emu/g (Gd) at 50 K and 300 K, respectively. The M_r residual magnetization and H_c coercive force were also determined, while the SQR loop squareness, k magnetic crystallographic anisotropy coefficient, and H_a anisotropy field were calculated. Temperature magnetization was measured in a field of 30 kOe. ZFC and FC magnetization curves were fixed in a field of 100 Oe. It was discovered that the T_{mo} magnetic ordering temperature downward-curve decreased from ~137.98 K (Sm) down to ~133.99 K (Gd). The spin glass state with ferromagnetic nanoinclusions for all the samples was observed. The <D> average and D_{max} maximum diameter of ferromagnetic nanoinclusions were calculated and they were in the range of 40–50 nm and 160–180 nm, respectively. The mechanism of magnetic state formation is discussed in terms of the effects of the A-site cation size and B-site poly-substitution on the indirect superexchange interactions.

Keywords: transition metals; crystal structure; high entropy perovskites; magnetic properties; indirect superexchange interactions

1. Introduction

Complex oxides based on transition metal cations have been the object of close research because of their fundamental importance and applied value for more than 70 years [1]. Among the specified class of compounds, the most promising are oxides with a perovskite structure [2]. This is due to their rich properties that allow them to be used as multifunctional materials [3]. The so-called multiferroics [4] are of great practical importance; multifunctional compounds simultaneously possessing two or more ferroic orderings are amenable to controlled change by coupled fields [5]. This behavior is especially important when solving problems of the induction, conversion, accumulation, and storage of electromagnetic energy [6].

The brightest representatives of perovskites are the $BaTiO_3$ barium titanate with well-known ferroelectric properties [7], the doped $Re_{1-x}A_xMn_{1-y}B_yO_3$ rare-earth orthomanganites with colossal magnetoresistance, and a diverse magnetic phase state [8]. The electrical and magnetic properties of the manganites are determined by the Mn^{3+}-O^{2-}-Mn^{3+} indirect superexchange interactions [9,10] associated with virtual transitions of the localized e_g electrons between Mn^{3+} cations [11] and with the special role of Jahn–Teller distortions of oxygen octahedra around the Mn^{3+} cation [12]. The intensity of the Mn^{3+}-O^{2-}-Mn^{3+} indirect superexchange interactions constantly increases with the $\langle Mn^{3+}\text{-}O^{2-}\text{-}Mn^{3+}\rangle$ average bond angle to 180 degrees and with the decrease in the $\langle Mn^{3+}\text{-}O^{2-}\rangle$ average bond length [13].

The degree of structural disorder in condensed matter determines such a thermodynamic parameter as entropy [14]. The most effective change in entropy depends on the cationic composition and location in the unit cell. Until recently, entropy was not considered as effective as enthalpy in materials development [15].

As is well known, the phase stability of a solid solution is determined by the change in the Gibbs free energy [16]. This change consists of a positive change in the mixing enthalpy and a negative change in the mixing entropy multiplied by the absolute temperature. With an increase in the mixing entropy, the change in the Gibbs free energy decreases, which leads to the stabilization of the phase state of the solid solution. The mixing entropy of a solid solution is determined by the number of mixing elements, the concentration of mixing elements, and the absolute temperature [17]. For each specific temperature, the value of entropy is maximum for a solid solution with an equal concentration of mixing elements, when the number of such elements rises upward [18]. It is generally accepted from practice that solid solutions containing more than five elements of the same type with a concentration of 20% should be classified as high-entropy ones [19]. It follows from this that the condition for the existence of a high-entropy solid solution is that the entropy exceeds the value of $1.61 \times R$, where R is the universal gas constant [20]. Such compounds demonstrate a unique combination of composition, structure, and physicochemical properties [21]. The most popular among high-entropy compounds are high-entropy oxides [22].

For the oxide perovskites, the production of high-entropy solid solutions is reduced to the substitution of at least five components in the A or B sublattice [23]. Such substitutions have two consequences: first, a structural consequence, where there is a change in the average radius of the corresponding sublattice and the associated possible removal of the cooperative static Jahn–Teller effect in the case of substitution in the B sublattice for the orthomanganites [24]; and secondly, an exchange consequence, where there is the weakening of exchange interactions associated with magnetic dilution [25]. Therefore, in the case of obtaining a high-entropy solid solution of perovskite with multicomponent substitution in the B sublattice, one should expect, along with an increase in phase stability, a weakening of the magnetic properties.

In the present paper, the Sm(Eu,Gd)$Cr_{0.2}Mn_{0.2}Fe_{0.2}Co_{0.2}Ni_{0.2}O_3$ high-entropy solid solutions were prepared by the usual ceramic technology and were investigated by XRD, SEM, and SQUID magnetometry. Effects of the A-site cation size and B-site poly-substitution on the Mn^{3+}(Cr^{3+}, Fe^{3+}, Co^{3+}, Ni^{2+})-O^{2-}-Mn^{3+}(Cr^{3+}, Fe^{3+}, Co^{3+}, Ni^{2+}) indirect superexchange interactions and magnetic properties were also studied.

2. Materials and Methods

Synthesis and Characterization

The samples of the three compositions of Sm(Eu,Gd)$Cr_{0.2}Mn_{0.2}Fe_{0.2}Co_{0.2}Ni_{0.2}O_3$ with the perovskite structure were synthesized using the usual ceramic technology. The high-purity (99.999%) rare-earth oxides of Sm_2O_3, Eu_2O_3, and Gd_2O_3, as well as the high-purity (99.999%) 3d metal oxides of Cr_2O_3, Mn_2O_3, Fe_2O_3, CoO, and NiO (CAS 1313-99-1, Luoyang Tongrun Nano Technology Co. Ltd., Luoyang, China), were used as the starting reagents. The chemical reaction of synthesis may be written as:

$$0.1Cr_2O_3 + 0.1Mn_2O_3 + 0.1Fe_2O_3 + 0.2CoO + 0.2NiO + 0.5Sm(Eu,Gd)_2O_3 + 0.2O_2 \rightarrow Sm(Eu,Gd)Cr_{0.2}\ Mn_{0.2}Fe_{0.2}Co_{0.2}Ni_{0.2}O_3 \quad (1)$$

The mixed powders of the required composition were grounded during 3 h in a ball mill with added alcohol. After this, the mixes were pressed in the form of 0.5 cm × 1 cm cylindrical pellets under a pressure of 3 tons/cm^2. Further, the samples were calcined at 1400 °C in air during 5 h followed by slow cooling down to room temperature [26].

XRD (Rigaku Ultima IV) (Rigaku Europe SE, Neu-Isenburg, Germany) with Cu-K_α radiation was used to check the phase content and calculate the unit cell parameters at room temperature. The angular scanning range was 20–90° with a rate of 1°/min. The Rietveld refinement [27] of XRD data in the frame of the Fullprof computer program (PROGRAM FullProf.2k (Version 7.40-March2021-ILL JRC), https://www.ill.eu/sites/fullprof/php/programs8809.html?pagina=FullProf (accessed on 18 December 2021)) [28] was used. The chemical composition was checked by EDX (Oxford INCA X-max 80) (Oxford Instruments, Moscow, Russian Federation). SEM was applied to obtain the microstructure images. SmartSEM (SmartSEM V05.06) software (Carl Zeiss SMT GmbH, Oberkochen, Germany) was used to treat three SEM images and to determine the average particle size for each sample [29].

The magnetization measurements were realized using a SQUID magnetometer [30]. The M(H) field magnetization loop was obtained in the range of 30−−30 kOe at 50 K and 300 K. The law of approach to saturation [31] was used to determine the M_s spontaneous magnetization. The M_r residual magnetization, SQR = M_r/M_s squareness of the loop, and H_c coercive force were determined. The k magnetic crystalline anisotropy coefficient and H_a anisotropy field were calculated. The temperature magnetization was measured in the range of 50–300 K in a field of 30 kOe. The point of minimum of the dM/dT(T) magnetization derivative or zero of the d^2M/dT^2(T) second magnetization derivative was taken as the T_{mo} magnetic ordering or T_c Curie temperature [32].

3. Results and Discussion

3.1. Crystal Structure

The phase purity and refinement of the unit cell parameters of the three obtained solid solutions were realized using X-ray powder diffraction at room temperature. The initial experimental data, as well as the results of the Rietveld fitting using the FullProf program, are shown in Figure 1. It is clearly seen that the results of matching the structural parameters within the Pnma (No. 62) space group give satisfactory results, as evidenced by the shape of the difference curve. When refining the unit cell parameters and ion coordinates, the χ^2 fitting goodness parameter does not exceed 2.5.

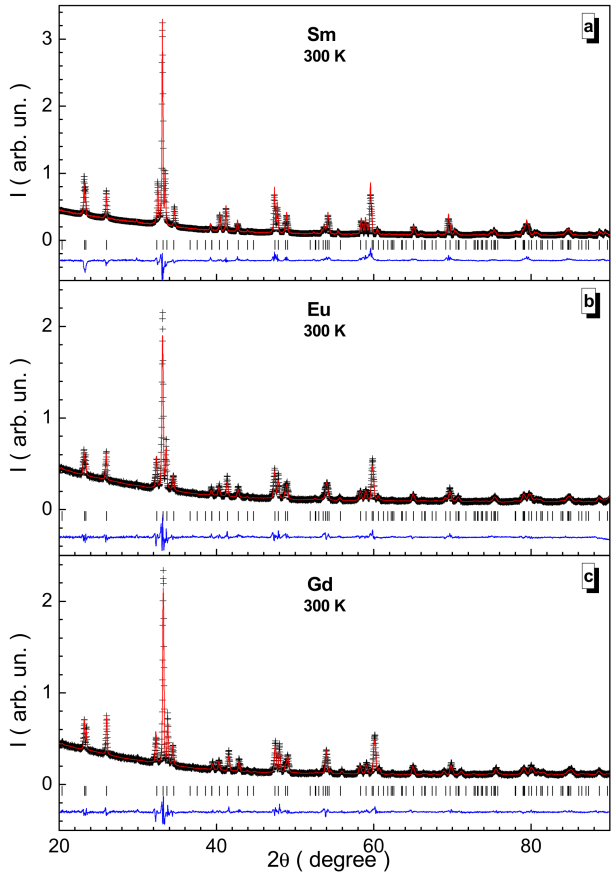

Figure 1. Rietveld-refined XRD pattern for the Sm- (**a**), Eu- (**b**), and Gd-based (**c**) samples. The experimental data (cross), fitting curve (red line), theoretical Bragg positions (vertical bar), and difference curve (blue line) are presented.

The unit cell parameters change monotonically and almost linearly. However, they have a multidirectional character of change with an increase in the serial number of the rare-earth cation. Thus, the *a* and *c* parameters decrease, and the *b* parameter increases (see Figure 2a). The maximum value of the *a* parameter is fixed for the samarium sample and is ~5.352 Å. The maximum value of the *b* parameter is fixed for the gadolinium sample and it is ~5.530 Å. The relative decreases in the *a* and *c* parameters are ~1.1 and ~0.7%, respectively, when going from the Sm^{3+} cation to the Gd^{3+} cation, while the relative increase in the *b* parameter is ~0.5%. The maximum V unit cell volume is observed for the samarium sample and is ~224.33 $Å^{3+}$. It decreases by ~1.3% when going to the Gd^{3+} cation.

It should be noted here that the Mn^{3+} cations in the octahedral environment of the O^{2-} oxygen anions are the Jahn–Teller ones, as their doubly degenerated e_g electron orbital is half-filled. All the cations participating in the formation of the studied solid solutions have an oxidation state of 3+. This follows from the laws of conservation of electric charge and electroneutrality of macroscopic bodies when the solid solution is stoichiometric. Of all the cations present with the oxidation state 3+ in the octahedral anionic coordination, only the Mn^{3+} manganese cation is the Jahn–Teller one.

Among the considered cations, the Jahn–Teller cations in an octahedral environment can also be cations of a triply charged Ni^{3+} nickel cation, which has 7 d electrons, in a high-spin state, and a triply charged Co^{3+} cobalt cation, which has 6 d electrons, in an intermediate spin state. Strictly speaking, it is theoretically possible to admit the observation of various combinations of oxidized states for the considered 3d transition metal cations at anionic stoichiometry, such as 3+-3+-3+-2+-4+ and 3+-2+-4+-2+-4+. However, the nickel cation, when synthesized in an air atmosphere, has a stable tendency to form the 2+ oxidized state. Then, for charge compensation, the transition of other used cations into the

4+ oxidized state is required. In this case, this can most likely be observed for the manganese cation. However, as the value of the electron affinity for the considered chemical elements is close to each other, it is possible to admit the development of such a situation only in a certain approximation. Moreover, each type of cation can have different oxidation states, i.e., the so-called charge disproportionation state can be observed. This further complicates the problem and it is clear that its solution requires additional theoretical and experimental studies.

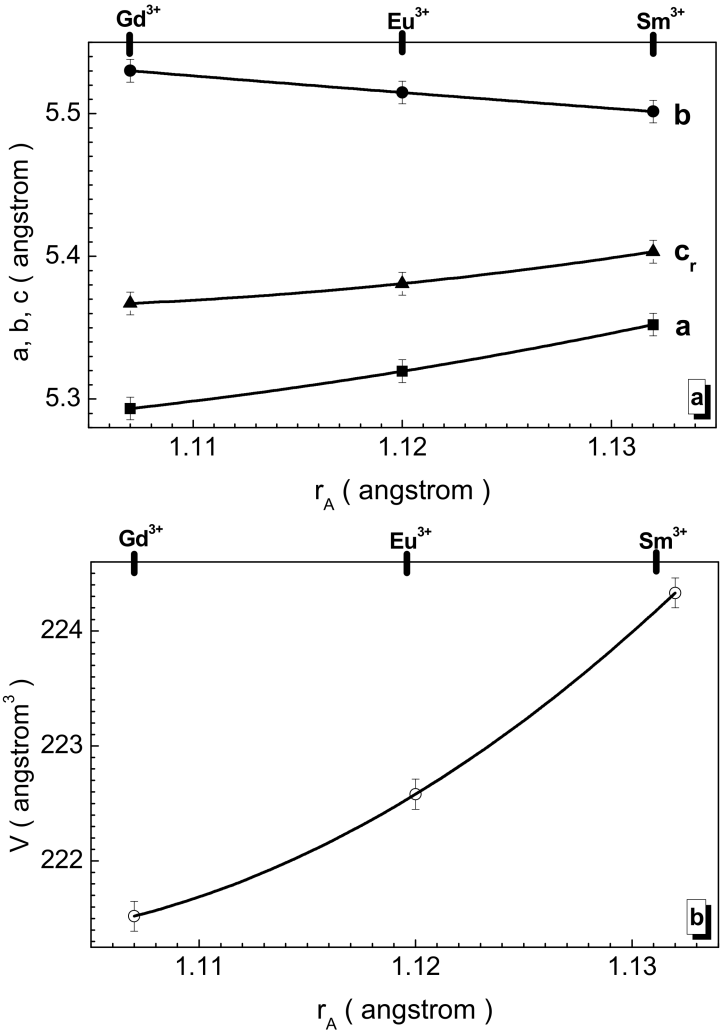

Figure 2. Dependence of unit cell parameters (**a**) a (full rectangle), b (full circle), and c/ $\sqrt{2}$ = c_r (full up-triangle), as well as unit cell volume (**b**) V (open circle) vs. A-site cation radius for the obtained samples. Solid line is the second-order polynomial interpolation and it is an eye guide.

Therefore, complex manganese oxides with a perovskite-like structure are often characterized by the Jahn–Teller effect. The latter manifests itself in the polar distortion of the oxygen octahedron. Two bond lengths become longer or shorter than the remaining four. The specific behavior and distortion of the unit cell observed in the samples under study is quite well explained by the size factor of the rare-earth cations filling the A positions in the perovskite structure and the absence of the cooperative static Jahn–Teller distortions. The absence of the cooperative static Jahn–Teller distortions is indicated by the observed O-orthorhombic symmetry of the unit cell. This type of distortion is characterized by a certain sequence of the unit cell parameters, which is as follows (a < c/$\sqrt{2}$ < b) [33]. In the presence of the cooperative static Jahn–Teller distortions, the sequence of the unit

cell parameters changes ($c/\sqrt{2} < a \leq b$), which indicates the formation of the so-called $O^{/}$-orthorhombic symmetry [34].

3.2. Microstructure

The surface images of the obtained ceramic samples presented in Figure 3 by the SEM method demonstrate a dense microstructure of granules of irregular shape and different sizes. As the serial number of the rare-earth cation increases, the maximum grain size decreases. Thus, for a samarium sample, the maximum grain size reaches ~17 μm; for a europium sample, it reaches ~16 μm, while, for a gadolinium sample, it reaches only ~13 μm.

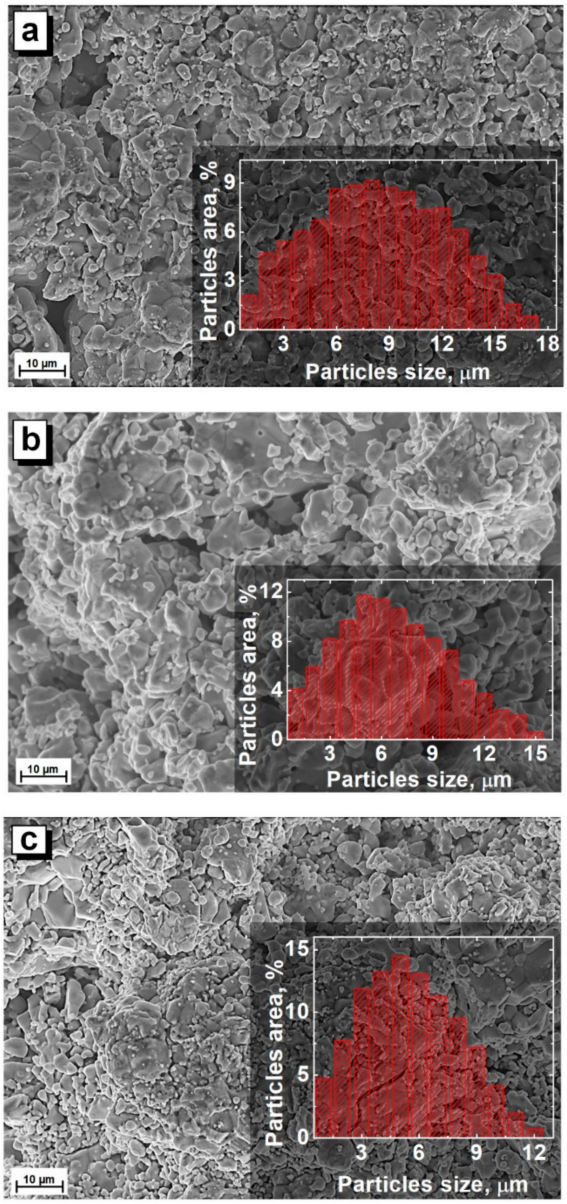

Figure 3. SEM image for the Sm- (**a**), Eu- (**b**), and Gd-based (**c**) samples. Inset demonstrates the particle size distribution.

Grains with sizes above these values were not observed. The relative fraction of grains from their total number with minimum sizes up to 1 μm was ~2, ~4, and ~5% for samarium, europium, and gadolinium samples, respectively, while the relative fraction of grains with maximum sizes reached only 1%. The maximum relative fraction of grains, which was ~9,

~12, and ~15% for samarium, europium, and gadolinium samples, reached sizes of ~8, ~5, and ~5 μm, respectively. The average grain size was in the range of 5–8 μm.

3.3. Magnetic Properties

From Figure 4, two main features are clearly visible. The first is that with an increase in the serial number of the rare-earth cation, the spontaneous magnetization increases; moreover, for the gadolinium sample, it increases significantly. The second is that with increasing temperature, the spontaneous magnetization decreases accordingly.

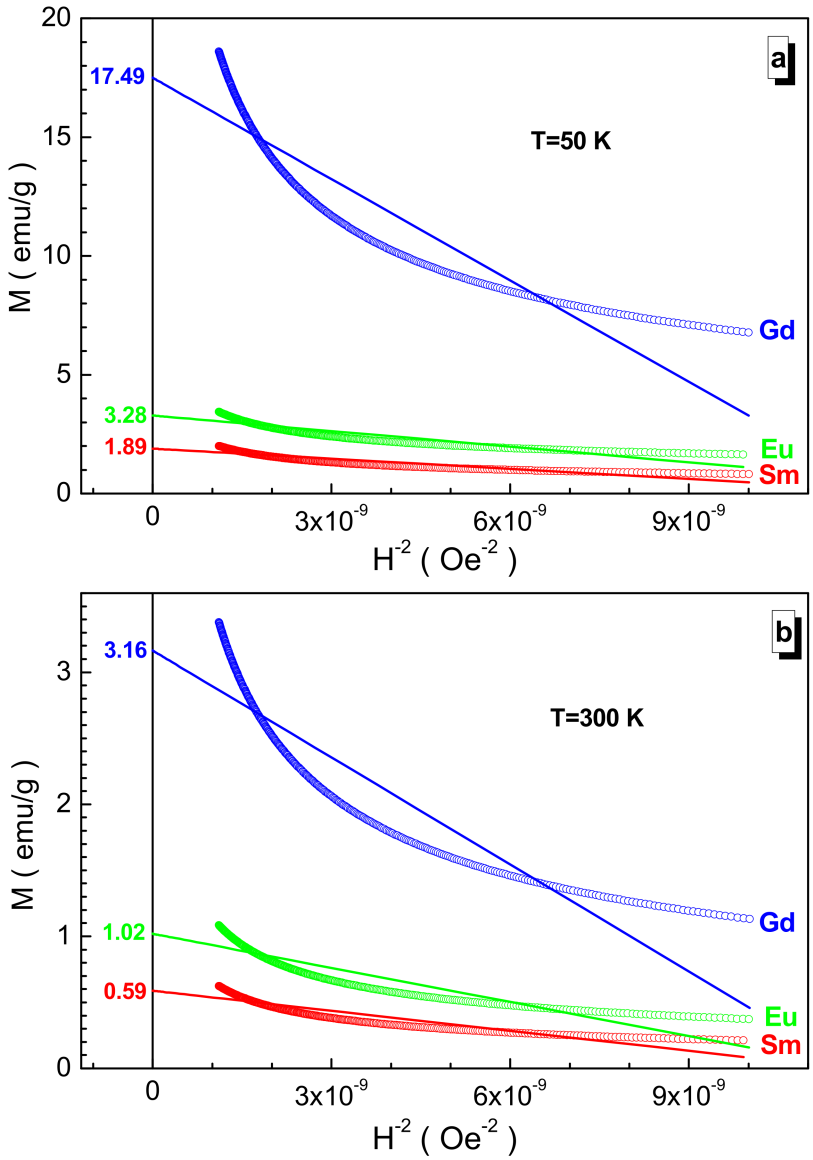

Figure 4. Dependence of magnetization vs. inverse square of the field for the Sm- (red circle), Eu- (green circle), and Gd-based (blue circle) samples at 50 K (**a**) and 300 K (**b**). Straight line is the linear extrapolation.

These two features are explained by the enhancement of the $Mn^{3+}(Cr^{3+}, Fe^{3+}, Co^{3+}, Ni^{2+})$-$O^{2-}$—$Mn^{3+}(Cr^{3+}, Fe^{3+}, Co^{3+}, Ni^{2+})$ indirect superexchange interactions as a result of a decrease in the $\langle Mn^{3+}(Cr^{3+}, Fe^{3+}, Co^{3+}, Ni^{2+})\text{-}O^{2-}\rangle$ average bond length of B-cations and an increase in the disordering action of thermal energy. The minimum value of the spontaneous magnetization is observed for the samarium sample, which is ~1.89 emu/g

at 50 K and ~0.59 emu/g at 300 K. This value increases when going to the Gd^{3+} cation by ~825% at 50 K and by ~436% at 300 K.

From the shape of the hysteresis loop in Figure 5, it can be concluded that for all the samples, there is a noticeable residual magnetization and coercive force, and with increasing temperature, they noticeably decrease. The maximum value of the residual magnetization of ~0.72 emu/g is observed for the gadolinium sample at 50 K, which decreases by ~73% when going to the samarium sample. The maximum value of the coercive force of ~2.81 Oe is observed for the samarium sample at 50 K, which decreases by ~67% upon passing to the gadolinium sample. This is due to the disordering of local spins by thermal energy and the destruction of domain walls.

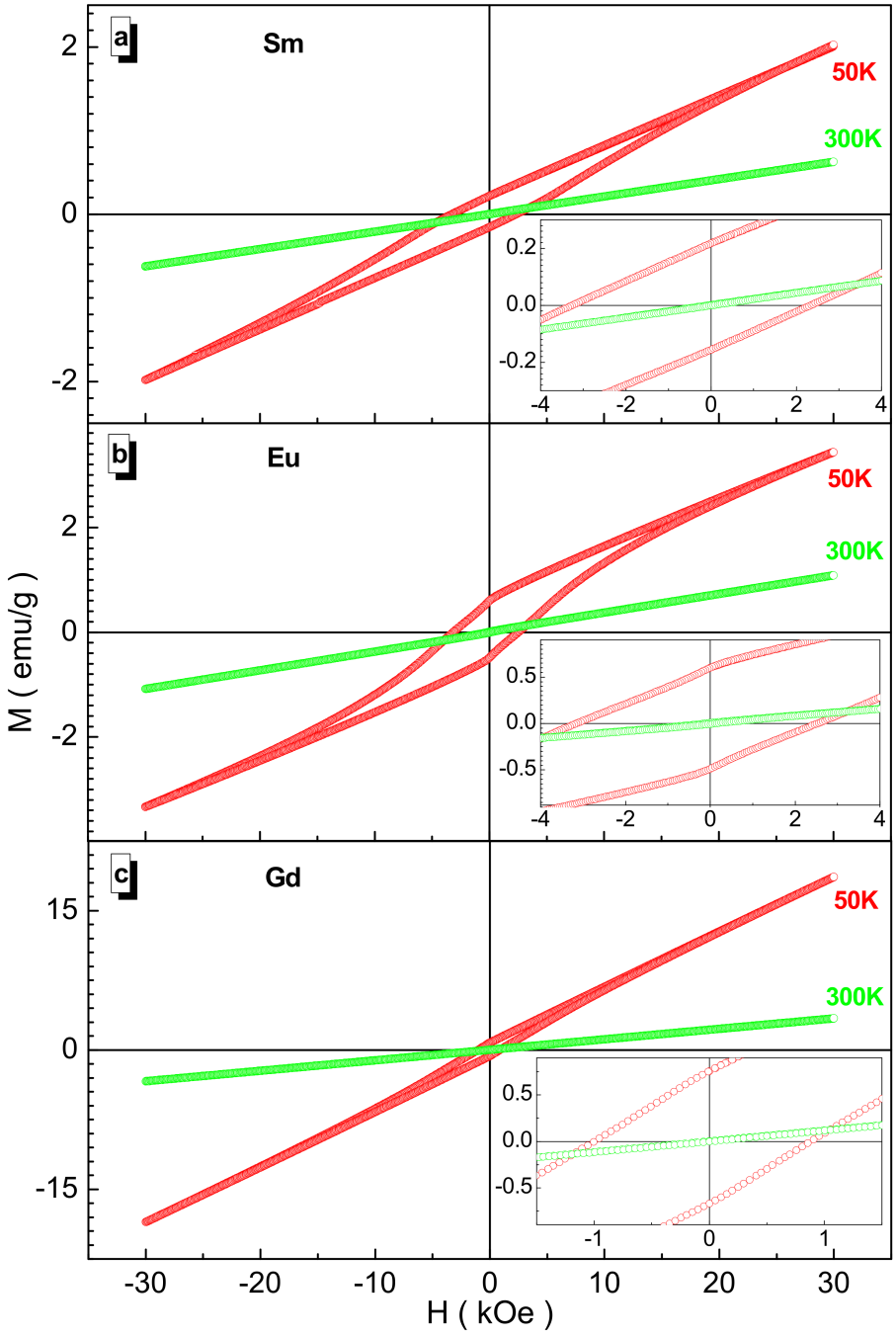

Figure 5. Field magnetization for the Sm- (**a**), Eu- (**b**), and Gd-based (**c**) samples at 50 K (red circle) and 300 K (green circle). Inset demonstrates the field magnetization on a larger scale.

The generalized dependences of the magnetic parameters taken from the field magnetization depending on the rare-earth cation size are shown in Figure 6. Almost all of these parameters do not change monotonically, that is, they have an inflection point with the exception of the spontaneous magnetization at both temperatures and residual magnetization at 50 K. All the low-temperature parameters are dominant. The maximum loop squareness observed for the europium sample is small and tends to ~0.17 at 50 K.

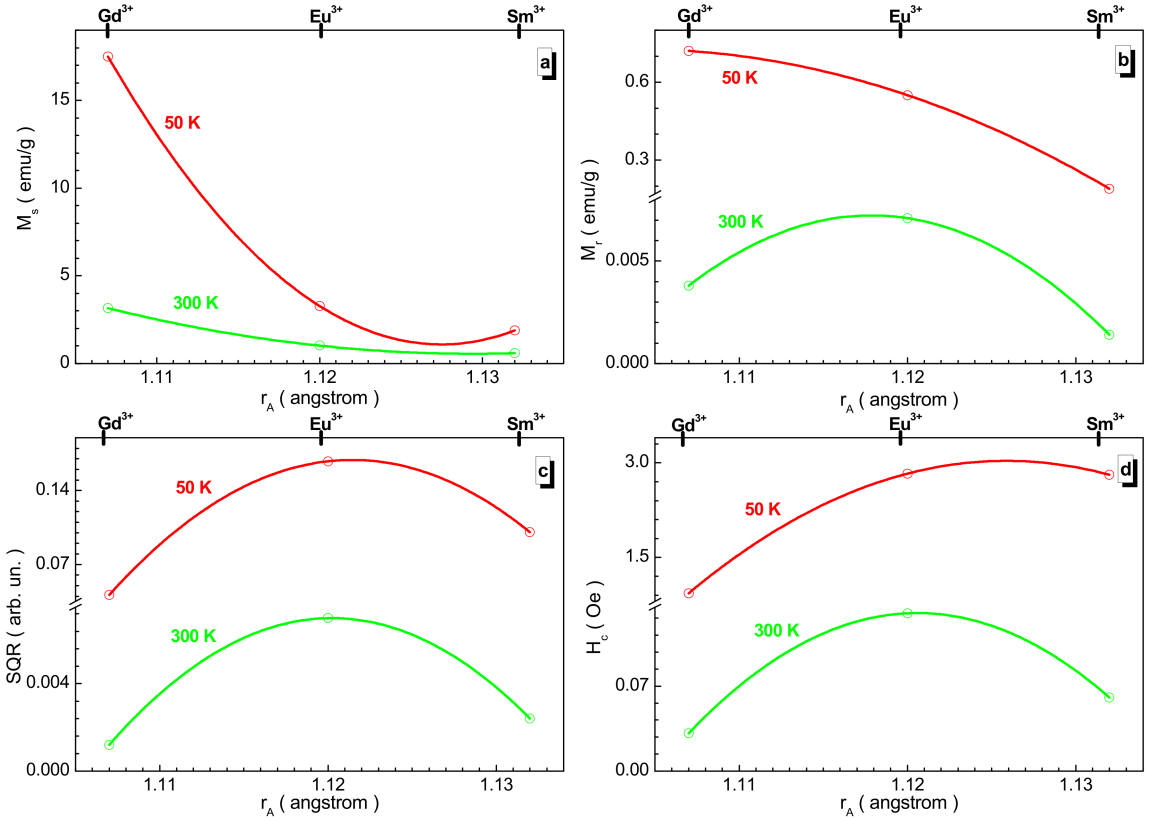

Figure 6. Dependence of the M_s spontaneous magnetization (**a**), M_r residual magnetization (**b**), SQR = M_r/M_s squareness of the loop (**c**), and H_c coercive force (**d**) vs. A-site cation radius size at 50 K (red circle and line) and 300 K (green circle and line) for the obtained samples. The solid line is the second-order polynomial interpolation and it is an eye guide.

Figure 7 shows the temperature dependences of magnetization in a strong field for the studied samples. They decrease almost monotonously with the field. Only for samarium and europium samples is an anomaly observed in the region of ~100–140 K. Such a constant decrease in magnetization means a diffuse phase transition to the paramagnetic state, which is characteristic of partially frustrated spin systems when clusters with different degrees of local spin ordering are present. It is the gradual disordering of these clusters that causes the smearing of the magnetic phase transition. To characterize this state, the magnetic ordering temperature was used, which is the point of maximum decrease in the corresponding function graph [35]. This magnetic ordering temperature was determined by the differential method from the extrema of the dM/dT(T) first derivative or from the zeros of the $d^2M/dT^2(T)$ second derivative of the M(T) magnetization. The maximum T_{mo} magnetic ordering temperature of ~134 K was recorded for the gadolinium sample, and the minimum T_{mo} of ~124 K was found for the europium sample. The anomalies for the samarium sample at ~58 K and ~106 K are most likely associated with the disordering of antiferromagnetic clusters formed by indirect superexchange interactions from the $Mn^{3+}(Cr^{3+}, Fe^{3+}, Co^{3+}, Ni^{2+})$-$O^2$-$Ni^{2+}$ (Mn^{3+}, Cr^{3+}, Fe^{3+}, Co^{3+}) set [36].

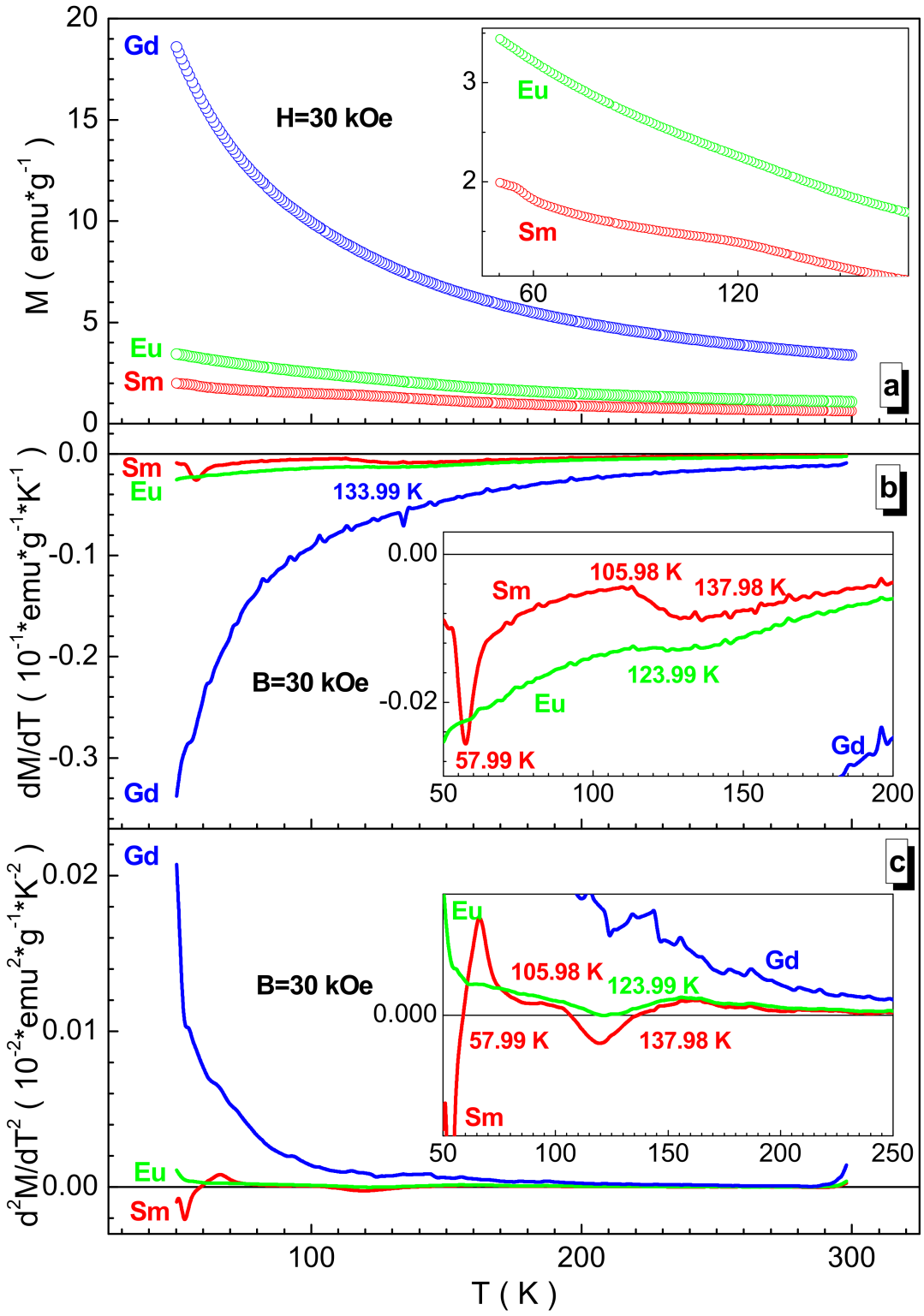

Figure 7. M(T) temperature magnetization (**a**), dM/dT(T) first magnetization derivative (**b**), and d^2M/dT^2(T) second magnetization derivative for the Sm- (red circle), Eu- (green circle) (**c**), and Gd-based (blue circle) samples in 3 T. Inset demonstrates the temperature magnetization on a larger scale.

The orthoferrites have the highest magnetic ordering temperature among all the complex 3d transition metal oxides used in this work. The $SmFeO_3$ samarium orthoferrite is a canted G-type antiferromagnet and their T_N Néel temperature reaches ~680 K [37]. It is interesting that the disordering temperature of the competing exchange between the

f- and d-electrons of the Sm^{3+} samarium and Fe^{3+} iron cations reaches ~140 K [38]. With an increase in the serial number of the rare-earth cation, the samples are characterized by a decrease in the magnetic ordering temperature [39] with the dominant Fe^{3+}-O^{2}-Fe^{3+} antiferromagnetic interactions and weak ferromagnetism due to the low-temperature ordering of the rare-earth magnetic sublattice [40].

The $SmMnO_3$ samarium manganite is an inhomogeneous A-type antiferromagnet [41] with the magnetic ordering temperature just below 90 K [42]. As the serial number of the rare-earth cation increases, the magnetic ordering temperature gradually decreases [43]. For the $EuMnO_3$ europium manganite, it is only T_{mo}~57 K [44]. For the $GdMnO_3$ gadolinium manganite, it is T_{mo}~51 K [45].

The perovskites based on the remaining rare-earth cations have even weaker magnetic properties. Thus, the magnetic state of the $SmCoO_3$ samarium orthocobaltite is complicated by the presence of spin phase separation under various external conditions. Near the ~500 K metal–dielectric transition, it is known [46]. This is explained by a change in the spin state of the Co^{3+} cobalt cation [47], which is determined by such parameters as the local crystal structure, the composition of substituents, and applied external fields such as thermal, baric, magnetic, and electric. Regardless of the crystal structure phase, the $SmCoO_3$ samarium orthocobaltite becomes metallic, as there is no forbidden band at the Fermi level. Thus, the orthorhombic phase becomes metallic when it has an A-type or C-type antiferromagnet structure, but remains semiconducting when the compound has a G-type antiferromagnet structure. Therefore, the metal–dielectric transition in the $SmCoO_3$ samarium orthocobaltite is not associated with the magnetic structure [48]. As the serial number of the rare-earth cation increases, the magnetic ordering temperature for the orthorhombic cobaltites decreases. Below room temperature, the main contribution to the magnetization is made by the paramagnetism of the rare-earth cations. The $SmCoO_3$ samarium orthocobaltite and $GdCoO_3$ gadolinium orthocobaltite are significantly different in magnetic terms. Such behavior is associated with differences in the structure of the electron shells of the rare-earth cations. For the $GdCoO_3$ gadolinium orthocobaltite, the magnetic behavior is close to the behavior of a set of free Gd^{3+} cations, while for the $SmCoO_3$ samarium orthocobaltite, a behavior more characteristic for bound cations is observed due to the fact that the ground state of Sm^{3+} is split by the crystal field of anions [49].

For the $SmCrO_3$ samarium orthochromite, three different magnetic phases are observed with decreasing temperature: first, there is an uncompensated canted antiferromagnetic structure that appears below the $T_N \approx 191$ K Néel temperature; second, a collinear antiferromagnetic structure that appears below ~10 K; and third, a nonequilibrium configuration with interacting phases in the vicinity of a spin-reorientation phase transition in the temperature range of 10 K $\leq T \leq$ 40 K [50]. With an increase in the serial number of the rare-earth cation in such canted antiferromagnetic structures as the orthocromites with a weak ferromagnetic component, the Néel temperature gradually decreases in the range from $T_N \approx 288$ K for the $LaCrO_3$ to $T_N \approx 112$ K for the $LuCrO_3$ [51].

It is difficult to characterize the magnetic structure and T_{mo} magnetic ordering temperature of the rare-earth orthonickelates, as these compounds are unstable in bulk due to the high oxygen pressure required to stabilize the nickel cation in the 3+ oxidation state [52]. Such stabilization can be achieved and maintained in multilayer thin-film structures, where each of the individual layers in their bulk form is unstable [53]. Such multilayer structures of the orthonickelates are characterized by complex antiferromagnetic ordering below the Néel temperature, which, for the $SmNiO_3$ samarium orthonickelate, is $T_N \approx 225$ K, while, for the $NdNiO_3$ neodymium orthonickelate, it is only $T_N \approx 200$ K [54].

To clarify the nature of the magnetic phase state, an attempt was made to study the low-field dynamics of spins for the samples obtained. Figure 8 presents such data for the samarium sample. It is clearly seen that, depending on the magnetic prehistory, the behavior of the spins is strikingly different. The ZFC curve exhibits a maximum characteristic of the spin glass state. The T_f freezing temperature, which determines the average diameter of a ferromagnetically ordered inclusion in a paramagnetic or antiferromagnetic medium,

is ~53 K. According to the Bean–Livingstone ratio [55], this freezing temperature corresponds to the <D> average diameter of a ferromagnetically ordered inclusion equal to ~50 nm. The T_{div} divergence temperature of the ZFC and FC curves, which determines the D_{max} maximum diameter of a ferromagnetically ordered inclusion, is ~187 K. It corresponds to the diameter of the maximum ferromagnetically ordered inclusion equal to ~180 nm. These data correlate well for the same previously obtained type of high-entropy perovskites based on such rare-earth cations as La^{3+} and Nd^{3+}. It should be noted that the magnetic ordering temperature in a weak field is much lower and is only ~71 K for the samarium sample (see Figure 8b).

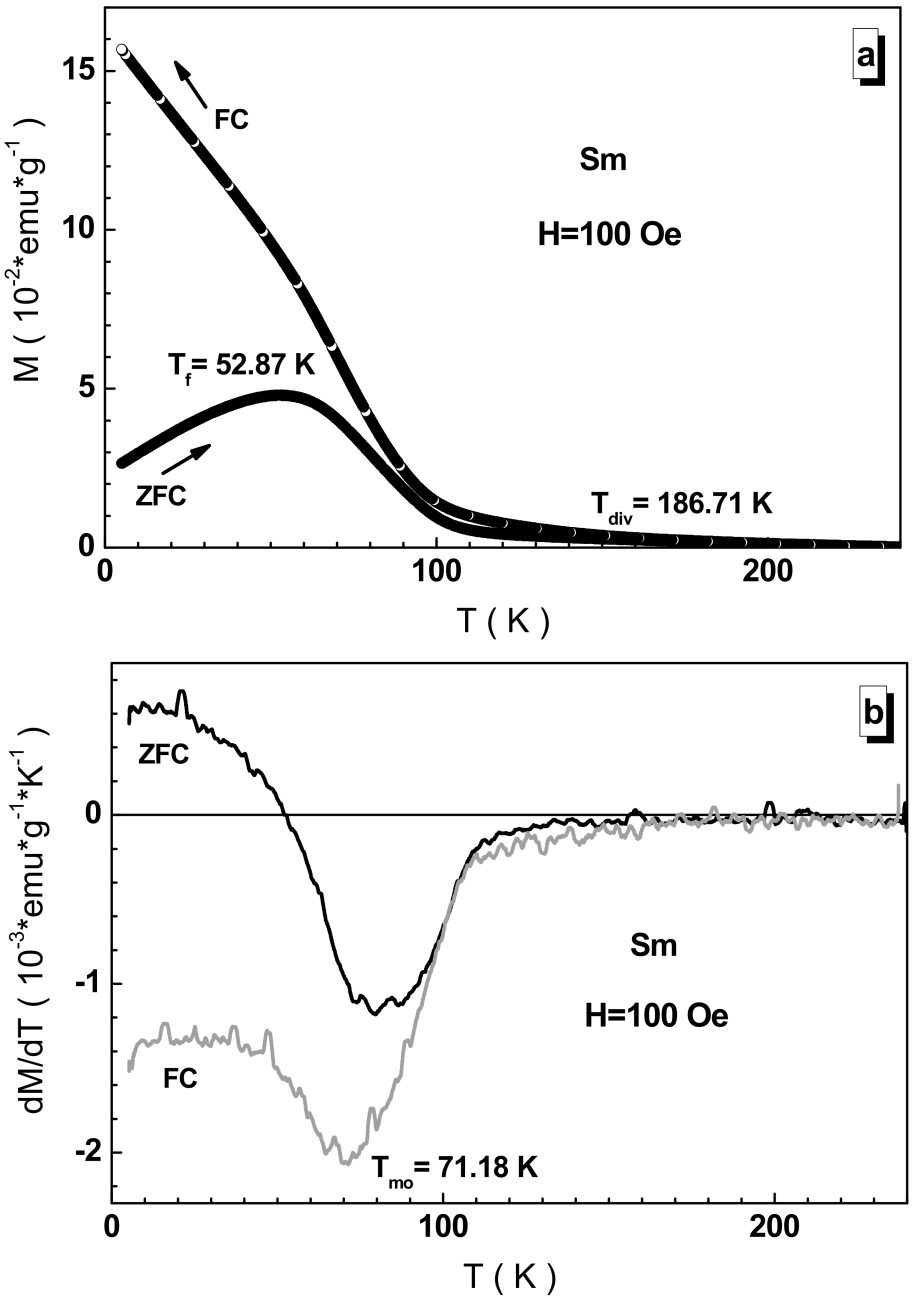

Figure 8. ZFC (full circle) and FC (open circle) curves of M(T) temperature magnetization (**a**) and their dM/dT(T) first magnetization derivative (**b**) for the Sm-based sample in 100 Oe. Inset demonstrates the temperature magnetization on a larger scale.

Figure 9 presents a summary of critical temperatures such as the freezing and magnetic ordering ones and the calculated magnetic parameters such as the k magnetic crystallographic anisotropy coefficient and anisotropy field. It can be seen that the critical temperatures have an oppositely directed behavior depending on the size of the rare-earth cation. The freezing temperature decreases monotonically from ~53 K for the samarium sample and decreases by ~14% for the gadolinium sample. At the same time, the magnetic ordering temperature passes through a local minimum for the europium sample, for which it is equal to ~124 K. The relative decrease in this temperature for the samarium sample from ~138 K to the gadolinium sample down to ~134 K is ~3%. For these temperatures, the corresponding average and maximum diameter of the ferromagnetic nanoinclusions are calculated, and they are in the range of 40–50 nm and 160–180 nm, respectively. The nonmonotonic behavior of the magnetic ordering temperature for the polysubstituted perovskites looks somewhat unusual, as, for each individual 3d cation [56], an increase in the magnetic ordering temperature, as a rule, the Néel temperature, and an increase in the spontaneous magnetization are observed as the serial number of the rare-earth cation increases [57].

Very often, in order to find materials with the required microwave parameters, it is necessary to know and optimize the anisotropic characteristics [58]. The magnetic properties of the high-entropy perovskite solid solutions obtained in this work will make it possible to select the required anisotropic parameters for the optimization of microwave materials in the future. This is the task of research in the near future.

In the approximation of uniaxial anisotropy, the calculation is quite simple [59]. Such data are presented in Figure 9b,c. The k magnetic crystallographic anisotropy coefficient increases almost monotonically as the seral number of the rare-earth cation increases at both temperatures. Thus, at 50 K, it increases from ~4.37×10^4 erg/g for the samarium sample by ~193% for the gadolinium sample, and at 300 K, it increases from ~8.09×10^3 erg/g for the samarium sample by ~1152% for the gadolinium sample. The H_a anisotropy field behaves in different directions at different temperatures [60–62]. Thus, at 50 K, it falls from ~14.6×10^4 Oe for the samarium sample by ~68% for the gadolinium sample, while, at 300 K, it increases from ~2.74×10^4 Oe for the samarium sample by ~133% for the gadolinium sample. This change in the behavior of the anisotropy field is explained by a sharp decrease in the spontaneous magnetization, which is dominant [63–65].

From the analysis of the above experimental information and already known literature data, it can be concluded that the investigated $Sm(Eu,Gd)Cr_{0.2}Mn_{0.2}Fe_{0.2}Co_{0.2}Ni_{0.2}O_3$ polysubstituted high-entropy perovskites are inhomogeneous antiferromagnets characterized by a magnetic state similar to the state of a spin glass with nanosized ferromagnetically ordered inclusions in an antiferromagnetic or paramagnetic medium and weak magnetic characteristics [66]. The complex substitution of B-cations in the perovskite cell increases the phase stability of the studied solid solutions, but decreases the magnetic parameters due to magnetic dilution and weakening of the $Mn^{3+}(Cr^{3+}, Fe^{3+}, Co^{3+}, Ni^{2+})$-$O^2$-$Mn^{3+}(Cr^{3+}, Fe^{3+}, Co^{3+}, Ni^{2+})$ indirect superexchange interactions. Reducing the size of the rare-earth cation has a stabilizing role due to the effect of chemical compression of the unit cell.

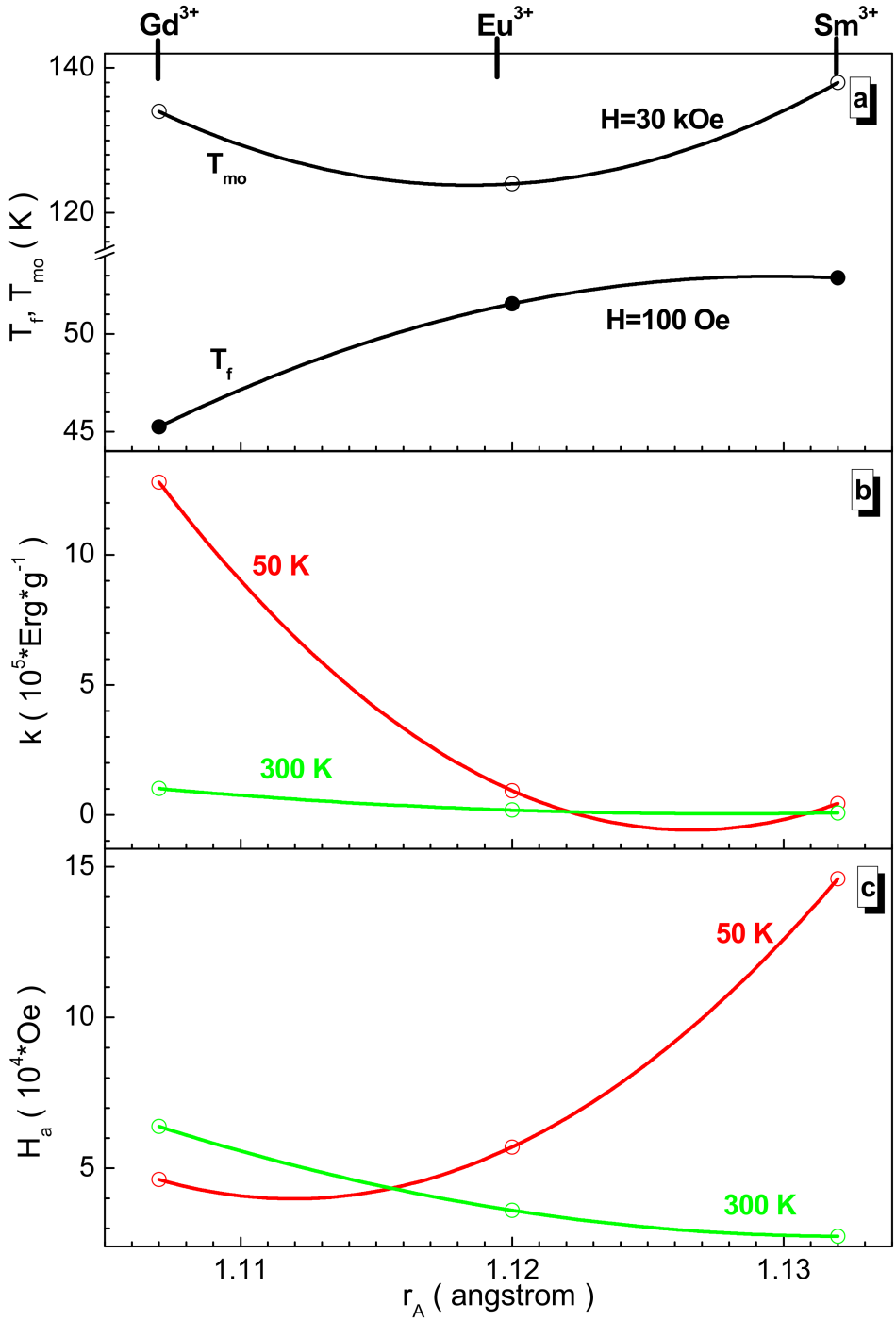

Figure 9. Dependence of the T_{mo} magnetic ordering (in 30 kOe) and T_f freezing (in 100 Oe) temperature (**a**), k magnetic crystallographic anisotropy coefficient (**b**), and H_a anisotropy field (**c**) vs. A-site cation radius size at 50 K (red circle and line) and 300 K (green circle and line) for the obtained samples. The solid line is the second-order polynomial interpolation and it is an eye guide.

4. Conclusions

Three high-entropy $Sm(Eu,Gd)Cr_{0.2}Mn_{0.2}Fe_{0.2}Co_{0.2}Ni_{0.2}O_3$ perovskite solid solutions were synthesized using the usual ceramic technology. The XRD investigation at room temperature established the single-phase perovskite product. The Rietveld refinement with the FullProf computer program in the frame of the orthorhombic Pnma (No 62) space group was realized. Along with a decrease in the V unit cell volume from ~224.33 $Å^3$ for the Sm-based sample down to ~221.52 $Å^3$ for the Gd-based sample, an opposite tendency

was observed for the unit cell parameters as the ordinal number of the rare-earth cation increased. The a and c unit cell parameters decreased from ~5.352 Å (Sm) and ~5.403 Å (Gd) down to ~5.293 Å (Sm) and ~5.367 Å (Gd), respectively, while the c unit cell parameter increased from ~5.502 Å (Sm) up to ~5.530 Å (Gd). The average grain size was in the range of 5–8 μm. Field magnetization was measured up to 30 kOe at 50 K and 300 K. The law of approach to saturation was used to determine the M_s spontaneous magnetization, which nonlinearly increased from ~1.89 emu/g (Sm) up to ~17.49 emu/g (Gd) and from ~0.59 emu/g (Sm) up to ~3.16 emu/g (Gd) at 50 K and 300 K, respectively. The M_r residual magnetization and H_c coercive force were also determined, while the SQR loop squareness, k magnetic crystallographic anisotropy coefficient, and H_a anisotropy field were calculated. The M_r residual magnetization nonlinearly increased from ~0.19 emu/g (Sm) up to ~0.72 emu/g (Gd) at 50 K. The H_c coercive force nonlinearly decreased from ~2.80 Oe (Sm) down to ~ 0.93 Oe (Gd) at 50 K. Temperature magnetization was measured in field of 30 kOe. ZFC and FC magnetization curves were fixed in a field of 100 Oe. It was discovered that the T_{mo} magnetic ordering temperature downward-curve decreased from ~137.98 K (Sm) down to ~133.99 K (Gd) in 30 kOe, while the T_f freezing temperature, on the contrary, upward-curve decreased from ~52.87 K (Sm) down to ~45.25 K. The spin glass state with ferromagnetic nanoinclusions for all the samples was observed. The <D> average and D_{max} maximum diameter of ferromagnetic nanoinclusions were calculated, and they were in the range of 40–50 nm and 160–180 nm, respectively. The mechanism of magnetic state formation was discussed in terms of the effects of the A-site cation size and B-site poly-substitution on the Mn^{3+}(Cr^{3+}, Fe^{3+}, Co^{3+}, Ni^{2+})-O^{2-}-Mn^{3+}(Cr^{3+}, Fe^{3+}, Co^{3+}, Ni^{2+}) indirect superexchange interactions.

Author Contributions: Conceptualization—D.A.V., S.V.T. (Sergey V. Taskaev), V.A.T., A.V.T. and S.V.T. (Sergei V. Trukhanov); methodology—V.E.Z., E.A.T., S.A.G., A.Y.P., M.G., O.V.Z., M.U.K. and D.A.B.; formal analysis—D.A.V., S.V.T. (Sergey V. Taskaev), M.U.K., A.A., D.A.B., M.I.S., A.V.T. and S.V.T. (Sergei V. Trukhanov); investigation—V.E.Z., A.Y.P., O.V.Z., A.V.T. and S.V.T. (Sergei V. Trukhanov); resources—D.A.V., E.A.T., S.A.G., S.V.T. (Sergey V. Taskaev), M.U.K., A.A., M.I.S. and V.A.T.; data curation—E.A.T., A.N.V., O.V.Z., M.I.S., A.V.T. and S.V.T. (Sergei V. Trukhanov); writing—original draft preparation—V.A.T., A.V.T. and S.V.T. (Sergei V. Trukhanov); review and editing—D.A.V., D.A.B., A.V.T. and S.V.T. (Sergei V. Trukhanov); visualization—V.E.Z., S.A.G., A.N.V., M.G. and A.A.; supervision—D.A.V., A.V.T. and S.V.T. (Sergei V. Trukhanov); project administration—E.A.T., V.A.T., A.V.T. and S.V.T. (Sergei V. Trukhanov); funding acquisition—D.A.V., S.A.G., D.A.B., M.I.S., A.V.T. and S.V.T. (Sergei V. Trukhanov). All authors have read and agreed to the published version of the manuscript.

Funding: The work was supported by the Russian Science Foundation (project No. 19-73-10046).

Data Availability Statement: Not applicable. Data could be shared upon reasonable request.

Conflicts of Interest: The authors declare no conflict of interest.

References

1. Zener, C. Interaction between thed-shells in the transition metals. II. ferromagnetic compounds of manganese with perovskite structure. *Phys. Rev.* **1951**, *82*, 403–405. [CrossRef]
2. Coey, J.M.D.; Viret, M.; Von Molnár, S. Mixed-valence manganites. *Adv. Phys.* **1999**, *48*, 167–293. [CrossRef]
3. Kubicek, M.; Bork, A.H.; Rupp, J.L.M. Perovskite oxides—A review on a versatile material class for solar-to-fuel conversion processes. *J. Mater. Chem. A* **2017**, *5*, 11983–12000. [CrossRef]
4. Fernández-Posada, C.; Castro, A.; Kiat, J.-M.; Porcher, F.; Peña, O.; Algueró, M.; Amorín, H. A novel perovskite oxide chemically designed to show multiferroic phase boundary with room-temperature magnetoelectricity. *Nat. Commun.* **2016**, *7*, 12772. [CrossRef]
5. Trukhanov, S.V.; Kostishin, V.G.; Panina, L.V.; Kazakevich, I.S.; Turchenko, V.; Kochervinskii, V.V. Coexistence of spontaneous polarization and magnetization in substituted M-type hexaferrites $BaFe_{12-x}Al_xO_{19}$ ($x \leq 1.2$) at room temperature. *JETP Lett.* **2016**, *103*, 100–105. [CrossRef]
6. Kostopoulou, A.; Kymakis, E.; Stratakis, E. Perovskite nanostructures for photovoltaic and energy storage devices. *J. Mater. Chem. A* **2018**, *6*, 9765–9798. [CrossRef]

7. Wang, P.-J.; Zhou, D.; Li, J.; Pang, L.-X.; Liu, W.-F.; Su, J.-Z.; Singh, C.; Trukhanov, S.; Trukhanov, A. Significantly enhanced electrostatic energy storage performance of P(VDF-HFP)/$BaTiO_3$-$Bi(Li_{0.5}Nb_{0.5})O_3$ nanocomposites. *Nano Energy* **2020**, *78*, 105247. [CrossRef]
8. Tokura, Y.; Tomioka, Y.; Kuwahara, H.; Asamitsu, A.; Moritomo, Y.; Kasai, M. Origins of colossal magnetoresistance in perovskite-type manganese oxides (invited). *J. Appl. Phys.* **1996**, *79*, 5288–5291. [CrossRef]
9. Trukhanov, S.V. Magnetic and magnetotransport properties of $La_{1-x}Ba_xMnO_{3-x/2}$ perovskite manganites. *J. Mater. Chem.* **2003**, *13*, 347–352. [CrossRef]
10. Trukhanov, S.V.; Troyanchuk, I.O.; Pushkarev, N.V.; Szymczak, H. Magnetic properties of anion-deficient $La_{1-x}Ba_xMnO_{3-x/2}$ ($0 \leq x \leq 0.30$) manganites. *J. Exp. Theor. Phys.* **2003**, *96*, 110–117. [CrossRef]
11. Goodenough, J.B. Theory of the role of covalence in the perovskite-type manganites [La, M(II)]MnO_3. *Phys. Rev.* **1955**, *100*, 564–573. [CrossRef]
12. Goodenough, J.B. Electronic structure of CMR manganites (invited). *J. Appl. Phys.* **1997**, *81*, 5330–5335. [CrossRef]
13. Cui, C.; Tyson, T.A.; Zhong, Z.; Carlo, J.P.; Qin, Y. Effects of pressure on electron transport and atomic structure of manganites: Low to high pressure regimes. *Phys. Rev. B* **2003**, *67*, 104107. [CrossRef]
14. Yeh, J.-W.; Chen, S.K.; Lin, S.-J.; Gan, J.-Y.; Chin, T.-S.; Shun, T.-T.; Tsau, C.-H.; Chang, S.-Y. Nanostructured high-entropy alloys with multiple principal elements: Novel alloy design concepts and outcomes. *Adv. Eng. Mater.* **2004**, *6*, 299–303. [CrossRef]
15. Cantor, B.; Chang, I.T.H.; Knight, P.; Vincent, A.J.B. Microstructural development in equiatomic multicomponent alloys. *Mater. Sci. Eng. A* **2004**, *375–377*, 213–218. [CrossRef]
16. Sarkar, A.; Wang, Q.; Schiele, A.; Chellali, M.R.; Bhattacharya, S.S.; Wang, D.; Brezesinski, T.; Hahn, H.; Velasco, L.; Breitung, B. High-entropy oxides: Fundamental aspects and electrochemical properties. *Adv. Mater.* **2019**, *31*, e1806236. [CrossRef] [PubMed]
17. McCormack, S.J.; Navrotsky, A. Thermodynamics of high entropy oxides. *Acta Mater.* **2020**, *202*, 1–21. [CrossRef]
18. Vinnik, D.; Trukhanov, A.; Podgornov, F.; Trofimov, E.; Zhivulin, V.; Starikov, A.; Zaitseva, O.; Gudkova, S.; Kirsanova, A.; Taskaev, S.; et al. Correlation between entropy state, crystal structure, magnetic and electrical properties in M-type Ba-hexaferrites. *J. Eur. Ceram. Soc.* **2020**, *40*, 4022–4028. [CrossRef]
19. Akrami, S.; Edalati, P.; Fuji, M.; Edalati, K. High-entropy ceramics: Review of principles, production and applications. *Mater. Sci. Eng. R Rep.* **2021**, *146*, 100644. [CrossRef]
20. Musicó, B.L.; Gilbert, D.; Ward, T.Z.; Page, K.; George, E.; Yan, J.; Mandrus, D.; Keppens, V. The emergent field of high entropy oxides: Design, prospects, challenges, and opportunities for tailoring material properties. *APL Mater.* **2020**, *8*, 040912. [CrossRef]
21. Sarkar, A.; Breitung, B.; Hahn, H. High entropy oxides: The role of entropy, enthalpy and synergy. *Scr. Mater.* **2020**, *187*, 43–48. [CrossRef]
22. Zhivulin, V.; Trofimov, E.; Gudkova, S.; Pashkeev, I.; Punda, A.; Gavrilyak, M.; Zaitseva, O.; Taskaev, S.; Podgornov, F.; Darwish, M.; et al. Polysubstituted high-entropy [LaNd]$(Cr_{0.2}Mn_{0.2}Fe_{0.2}Co_{0.2}Ni_{0.2})O_3$ perovskites: Correlation of the electrical and magnetic properties. *Nanomaterials* **2021**, *11*, 1014. [CrossRef]
23. Vinnik, D.A.; Trofimov, E.A.; Zhivulin, V.E.; Gudkova, S.A.; Zaitseva, O.V.; Zherebtsov, D.A.; Starikov, A.Y.; Sherstyuk, D.P.; Amirov, A.A.; Kalgin, A.V.; et al. High entropy oxide phases with perovskite structure. *Nanomaterials* **2020**, *10*, 268. [CrossRef]
24. Trukhanov, S.V.; Bushinsky, M.V.; Troyanchuk, I.O.; Szymczak, H. Magnetic ordering in $La_{1-x}Sr_xMnO_{3-x/2}$ anion-deficient manganites. *J. Exp. Theor. Phys.* **2004**, *99*, 756–765. [CrossRef]
25. Dang, N.; Zakhvalinskii, V.; Kozlenko, D.; Phan, T.-L.; Kichanov, S.; Trukhanov, S.; Nekrasova, Y.; Taran, S.; Ovsyannikov, S.; Jabarov, S.; et al. Effect of Fe doping on structure, magnetic and electrical properties $La_{0.7}Ca_{0.3}Mn_{0.5}Fe_{0.5}O_3$ manganite. *Ceram. Int.* **2018**, *44*, 14974–14979. [CrossRef]
26. Trukhanov, S.V.; Dang, N.T.; Zakhvalinskii, V.S.; Kozlenko, D.P.; Phan, T.-L.; Kichanov, S.; Ovsyannikov, S.V.; Jabarov, S.H.; Trukhanova, E.L.; Vinnik, D.; et al. Magnetotransport properties and phase separation in iron substituted lanthanum-calcium manganite. *Mater. Res. Express* **2018**, *5*, 086108. [CrossRef]
27. Rietveld, H.M. A profile refinement method for nuclear and magnetic structures. *J. Appl. Crystallogr.* **1969**, *2*, 65–71. [CrossRef]
28. Rodríguez-Carvajal, J. Recent advances in magnetic structure determination by neutron powder diffraction. *Phys. B Condens. Matter.* **1993**, *192*, 55–69. [CrossRef]
29. Turchenko, V.A.; Trukhanov, S.V.; Kostishin, V.G.; Damay, F.; Porcher, F.; Klygach, D.S.; Vakhitov, M.G.; Lyakhov, D.; Michels, D.; Bozzo, B.; et al. Features of structure, magnetic state and electrodynamic performance of $SrFe_{12-x}In_xO_{19}$. *Sci. Rep.* **2021**, *11*, 1–14. [CrossRef]
30. Trukhanov, S.V. Peculiarities of the magnetic state in the system $La_{0.70}Sr_{0.30}MnO_{3-\gamma}$ ($0 \leq \gamma \leq 0.25$). *J. Exp. Theor. Phys.* **2005**, *100*, 95–105. [CrossRef]
31. Grössinger, R. Correlation between the inhomogeneity and the magnetic anisotropy in polycrystalline ferromagnetic materials. *J. Magn. Magn. Mater.* **1982**, *28*, 137–142. [CrossRef]
32. Trukhanov, S.; Trukhanov, A.V.; Szymczak, H. Effect of magnetic fields on magnetic phase separation in anion-deficient manganite $La_{0.70}Sr_{0.30}MnO_{2.85}$. *Low Temp. Phys.* **2011**, *37*, 465. [CrossRef]
33. Trukhanov, S.V.; Vasiliev, A.; Balagurov, A.M.; Szymczak, H. Magnetic state of the structural separated anion-deficient $La_{0.70}Sr_{0.30}MnO_{2.85}$ manganite. *J. Exp. Theor. Phys.* **2011**, *113*, 819–825. [CrossRef]
34. Goodenough, J.B.; Wold, A.; Arnott, R.J.; Menyuk, N. Relationship between crystal symmetry and magnetic properties of ionic compounds containing Mn^{3+}. *Phys. Rev.* **1961**, *124*, 373–384. [CrossRef]

35. Topkaya, R. Effect of composition and temperature on the magnetic properties of $BaBi_xLa_xFe_{(12-2x)}O_{19}$ ($0.0 \leq x \leq 0.2$) hexaferrites. *Appl. Phys. A* **2017**, *123*, 488. [CrossRef]
36. Da Silva, C.A.; Silva, R.S.; Plaza, E.J.R.; Moreno, N.O. Magnetic state and magnetocaloric effect of $SmMnO_3$. *J. Supercond. Nov. Magn.* **2013**, *26*, 2497–2499. [CrossRef]
37. Cao, S.; Zhao, H.; Kang, B.; Zhang, J.; Ren, W. Temperature induced spin switching in $SmFeO_3$ single crystal. *Sci. Rep.* **2015**, *4*, srep05960. [CrossRef]
38. Marshall, L.G.; Cheng, J.; Zhou, J.-S.; Goodenough, J.B.; Yan, J.; Mandrus, D.G. Magnetic coupling between Sm^{3+} and the canted spin in an antiferromagnetic $SmFeO_3$ single crystal. *Phys. Rev. B* **2012**, *86*, 064417. [CrossRef]
39. Pinho, S.L.C.; Amaral, J.S.; Wattiaux, A.; Duttine, M.; Delville, M.; Geraldes, C.F.G.C. Synthesis and characterization of rare-earth Orthoferrite $LnFeO_3$ nanoparticles for bioimaging. *Eur. J. Inorg. Chem.* **2018**, *2018*, 3570–3578. [CrossRef]
40. Lone, I.; Aslam, J.; Radwan, N.R.E.; Bashal, A.H.; Ajlouni, A.F.A.; Akhter, A. Multiferroic ABO_3 transition metal Oxides: A rare interaction of ferroelectricity and magnetism. *Nanoscale Res. Lett.* **2019**, *14*, 1–12. [CrossRef]
41. Kimura, T.; Ishihara, S.; Shintani, H.; Arima, T.-H.; Takahashi, K.T.; Ishizaka, K.; Tokura, Y. Distorted perovskite with e_g^1 configuration as a frustrated spin system. *Phys. Rev. B* **2003**, *68*, 060403. [CrossRef]
42. Choi, E.-M.; Maity, T.; Kursumovic, A.; Lu, P.; Bi, Z.; Yu, S.; Park, Y.; Zhu, B.; Wu, R.; Gopalan, V.; et al. Nanoengineering room temperature ferroelectricity into orthorhombic $SmMnO_3$ films. *Nat. Commun.* **2020**, *11*, 2207–2209. [CrossRef] [PubMed]
43. Shimamoto, K.; Mukherjee, S.; Bingham, N.S.; Suszka, A.K.; Lippert, T.; Niedermayer, C.; Schneider, C.W. Single-axis-dependent structural and multiferroic properties of orthorhombic $RMnO_3$ (R = Gd–Lu). *Phys. Rev. B* **2017**, *95*, 184105. [CrossRef]
44. Kokila, I.P.; Kanagaraj, M.; Kumar, P.S.; Peter, S.C.; Sekar, C.; Therese, H.A. Structural, magnetic and magnetocaloric properties of $EuMnO_3$ perovskite manganite: A comprehensive MCE study. *Mater. Res. Express* **2018**, *5*, 026107. [CrossRef]
45. Modi, A.; Thakur, R.K.; Thakur, R.; Gaur, N.K. Magnetic transport behavior of multiferroic $GdMnO_3$. *AIP Conf. Proc.* **2015**, *1661*, 060003. [CrossRef]
46. Capon, F.; Boileau, A.; Carteret, C.; Martin, N.; Boulet, P.; Pierson, J.F. Cation size effect on the thermochromic properties of rare earth cobaltites $RECoO_3$ (*RE*: La, Nd, Sm). *J. Appl. Phys.* **2013**, *114*, 113510. [CrossRef]
47. Vasil'Chikova, T.N.; Kuz'Mova, T.G.; Kamenev, A.A.; Kaul', A.R.; Vasil'Ev, A.N. Spin states of cobalt and the thermodynamics of $Sm_{1-x}Ca_xCoO_{3-\delta}$ solid solutions. *JETP Lett.* **2013**, *97*, 34–37. [CrossRef]
48. Olsson, E.; Aparicio-Anglès, X.; De Leeuw, N.H. A DFT+U study of the structural, electronic, magnetic, and mechanical properties of cubic and orthorhombic $SmCoO_3$. *J. Chem. Phys.* **2016**, *145*, 224704. [CrossRef]
49. Ivanova, N.B.; Kazak, N.V.; Michel, C.; Balaev, A.D.; Ovchinnikov, S.G. Low-temperature magnetic behavior of the rare-earth cobaltites $GdCoO_3$ and $SmCoO_3$. *Phys. Solid State* **2007**, *49*, 2126–2131. [CrossRef]
50. Tripathi, M.; Choudhary, R.J.; Phase, D.M.; Chatterji, T.; Fischer, H.E. Evolution of magnetic phases in $SmCrO_3$: A neutron diffraction and magnetometric study. *Phys. Rev. B* **2017**, *96*, 174421. [CrossRef]
51. Oliveira, G.N.P.; Teixeira, R.C.; Moreira, R.P.; Correia, J.G.; Araújo, J.P.; Lopes, A.M.L. Local inhomogeneous state in multiferroic $SmCrO_3$. *Sci. Rep.* **2020**, *10*, 4686–4712. [CrossRef]
52. Demazeau, G.; Marbeuf, A.; Pouchard, M.; Hagenmuller, P. Sur une série de composés oxygènes du nickel trivalent derivés de la perovskite. *J. Solid State Chem.* **1971**, *3*, 582–589. [CrossRef]
53. Girardot, C.; Pignard, S.; Weiss, F.; Kreisel, J. $SmNiO_3/NdNiO_3$ thin film multilayers. *Appl. Phys. Lett.* **2011**, *98*, 241903. [CrossRef]
54. Medarde, M.L. Structural, magnetic and electronic properties of $RNiO_3$ perovskites (R = rare earth). *J. Phys. Condens. Matter* **1997**, *9*, 1679–1707. [CrossRef]
55. Bean, C.P.; Livingston, J.D. Superparamagnetism. *J. Appl. Phys.* **1959**, *30*, S120–S129. [CrossRef]
56. Troyanchuk, I.; Khalyavin, D.D.; Trukhanov, S.V.; Szymczak, H. Magnetic phase diagrams of the manganites $Ln_{1-x}Ba_xMnO_3$ (Ln = Nd, Sm). *J. Phys. Condens. Matter* **1999**, *11*, 8707–8717. [CrossRef]
57. Troyanchuk, I.; Khalyavin, D.D.; Trukhanov, S.V.; Szymczak, H.; Nabialek, A. Magnetotransport properties of the $Sm_{0.56}(Sr_{0.44-x}Me_x)MnO_3$ (Me = Ba, Ca, Cd) perovskites. *J. Phys. Condens. Matter* **1999**, *11*, 8913–8920. [CrossRef]
58. Almessiere, M.A.; Slimani, Y.; Güngüneş, H.; Korkmaz, A.D.; Zubar, T.; Trukhanov, S.; Trukhanov, A.; Manikandan, A.; Alahmari, F.; Baykal, A. Influence of Dy^{3+} Ions on the microstructures and magnetic, electrical, and microwave properties of $[Ni_{0.4}Cu_{0.2}Zn_{0.4}](Fe_{2-x}Dy_x)O_4$ ($0.00 \leq x \leq 0.04$) spinel ferrites. *ACS Omega* **2021**, *6*, 10266–10280. [CrossRef]
59. Herbst, J.F.; Pinkerton, F.E. Law of approach to saturation for polycrystalline ferromagnets: Remanent initial state. *Phys. Rev. B* **1998**, *57*, 10733–10739. [CrossRef]
60. Shlimas, D.I.; Kozlovskiy, A.L.; Zdorovets, M.V. Study of the formation effect of the cubic phase of $LiTiO_2$ on the structural, optical, and mechanical properties of $Li_{2\pm x}Ti_{1\pm}xO_3$ ceramics with different contents of the X component. *J. Mater. Sci. Mater. Electron.* **2021**, *32*, 7410–7422. [CrossRef]
61. Kozlovskiy, A.L.; Shlimas, D.I.; Zdorovets, M.V. Synthesis, structural properties and shielding efficiency of glasses based on TeO_2-(1-x)ZnO-xSm_2O_3. *J. Mater. Sci. Mater. Electron.* **2021**, *32*, 12111–12120. [CrossRef]
62. Kozlovskiy, A.; Egizbek, K.; Zdorovets, M.V.; Ibragimova, M.; Shumskaya, A.; Rogachev, A.A.; Ignatovich, Z.V.; Kadyrzhanov, K. Evaluation of the efficiency of detection and capture of manganese in aqueous solutions of FeCeOx nanocomposites doped with Nb_2O_5. *Sensors* **2020**, *20*, 4851. [CrossRef] [PubMed]

63. Zdorovets, M.V.; Kozlovskiy, A.L.; Shlimas, D.I.; Borgekov, D.B. Phase transformations in FeCo–Fe_2CoO_4/Co_3O_4-spinel nanostructures as a result of thermal annealing and their practical application. *J. Mater. Sci. Mater. Electron.* **2021**, *32*, 16694–16705. [CrossRef]
64. Kozlovskiy, A.L.; Zdorovets, M.V. Synthesis, structural, strength and corrosion properties of thin films of the type CuX (X = Bi, Mg, Ni). *J. Mater. Sci. Mater. Electron.* **2019**, *30*, 11819–11832. [CrossRef]
65. Zhumatayeva, I.Z.; Kenzhina, I.E.; Kozlovskiy, A.L.; Zdorovets, M.V. The study of the prospects for the use of $Li_{0.15}Sr_{0.85}TiO_3$ ceramics. *J. Mater. Sci. Mater. Electron.* **2020**, *31*, 6764–6772. [CrossRef]
66. Kozlovskiy, A.L.; Zdorovets, M.V. Effect of doping of $Ce^{4+/3+}$ on optical, strength and shielding properties of (0.5-x)TeO_2-0.25MoO-0.25Bi_2O_3-xCeO_2 glasses. *Mater. Chem. Phys.* **2021**, *263*, 124444. [CrossRef]